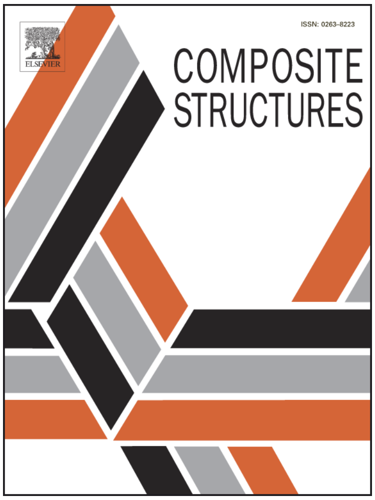

Autonomous structural health monitoring of composite wind turbine blades using guided waves and machine learning

Farbod Dadashbaki, Anjaly J. Pillai, Shirsendu Sikdar, Dianzi Liu, Karl Walton, Rakesh Mishra

PII: S0263-8223(25)01120-1
DOI: https://doi.org/10.1016/j.compstruct.2025.119955
Reference: COST 119955

To appear in: *Composite Structures*

Received Date: 14 July 2025
Revised Date: 21 November 2025
Accepted Date: 12 December 2025

Please cite this article as: Dadashbaki, F., Pillai, A.J., Sikdar, S., Liu, D., Walton, K., Mishra, R., Autonomous structural health monitoring of composite wind turbine blades using guided waves and machine learning, *Composite Structures* (2025), doi: https://doi.org/10.1016/j.compstruct.2025.119955

Autonomous Structural Health Monitoring of Composite Wind Turbine Blades using Guided Waves and Machine Learning

Farbod Dadashbaki[1], Anjaly J Pillai[2], Shirsendu Sikdar[1,*], Dianzi Liu[3], Karl Walton[1], and Rakesh Mishra[1]

[1]School of Computing and Engineering, University of Huddersfield, Huddersfield HD1 3DH, United Kingdom.

[2]Department of Civil Engineering, Amrita School of Engineering, Coimbatore, Amrita Vishwa Vidyapeetham, India.

[3]School of Engineering, Mathematica and Physics, University of East Anglia, Norwich, NR4 7TJ, United Kingdom.

[*]Corresponding Author: s.sikdar@hud.ac.uk

Abstract

This research paper presents a guided wave (GW)-driven framework for structural health monitoring of composite wind turbine blades, leveraging both experimental and numerical data in conjunction with a hybrid machine learning (ML) approach for accurate damage identification and classification. High-fidelity ultrasonic GW signals were collected under controlled laboratory conditions for pristine and damaged blade states, including erosion damage, longitudinal debonding, and transverse debonding. Finite element simulations, incorporating a tri-array of sensors, were further employed to enhance spatial resolution and replicate complex wave-damage interactions. All GW signals were converted into time-frequency representations using scalogram analysis, enabling rich feature encoding of frequency dispersion characteristics for each damage case. These scalogram images were used as input to a two-stage ML classifier based on transfer learning, which first performs binary damage detection, followed by multi-class classification of damage types. The proposed model achieved high classification accuracy across both synthetic and experimental datasets, with statistical confidence intervals confirming the robustness of predictions. This methodology demonstrates the viability of integrating physics-informed data with ML to enable automated, high-resolution health status monitoring of composite blades and supports its scalability for deployment in operational wind energy systems.

Keywords: guided waves; structural health monitoring; composite materials; wind turbine blades; machine learning; ultrasonic sensing.

1. Introduction

Wind energy has proved itself to be a notable contributor in the renewable sector, ranked by the International Energy Agency (IEA) as the second most prominent clean source after solar energy [1]. As the Global Wind Energy Council (GWEC) reported, the world's installed capacity for wind power reached an unprecedented record in 2024, adding approximately 117 gigawatts within a single year, which was enabled by new wind farms constructed in 54 countries. The share of wind energy in the renewable market is yet projected to triple by 2030 [2]. Accordingly, the accurate assessment of wind turbine structural anomalies using novel approaches seems more crucial to guarantee their reliable, cost-effective operation over the long run [3], [4].

Industry-grade wind turbines are not easy-to-access equipment as they are often tall structures, located far from each other within a remote area. In addition, they routinely operate in harsh environmental conditions, exposing their components to a broad span of damage conditions. For instance, ‘wake effects’ in diverse geographical regions under varying atmospheric conditions not only cause significant annual energy production (AEP) losses ranging from 28% to 45% [5], [6], but also compromise wind turbines’ structural integrity due to increasing fatigue loads in rotor blades by 5% to 15% [7], [8]. The operation and maintenance (O&M) costs for onshore wind turbines typically make up 12-30% of their total lifetime costs, while for offshore counterparts, these costs are reported to be around 32% or more [9]. Such figures indicate that early anomaly detection through innovative Structural Health Monitoring (SHM) is essential for ensuring that wind farms operate efficiently and safely, with minimum downtime and maintenance costs.

WTBs are commonly manufactured from composite materials like glass-fibre reinforced polymer (GFRP) because they are cost-effective and considerably light, while providing high strength [10]. On the other hand, these composite structures are highly likely to experience damage scenarios-e.g., delamination, debonding and crack-which are caused by manufacturing defects, varied loading, and environmental factors [11]. Moreover, damaged WTBs are difficult to recycle and frequently end up in large landfills, negatively affecting the environment [12]. WTBs can also directly impact wind turbine’s functionality. Therefore, they require continuous condition monitoring with high effectiveness and sensitivity [13], [14].

A wide range of non-destructive inspection and condition monitoring methods have been developed for WTBs, including vibration-based monitoring, acoustic emission (AE), infrared thermography, fibre-optic sensing, and ultrasonic guided wave (GW) propagation. Comparative reviews have summarized their performance in terms of sensitivity, detection depth, deployment requirements, and cost-effectiveness [15], [16], [17]. Although vibration-based methods can provide global indicators of blade health, they suffer from several limitations. First, they are often insensitive to small or incipient damage, as changes in modal properties only become measurable once defects reach a significant size [18]. Second, vibration signals are influenced by varying environmental and operational conditions (e.g., wind speed, rotor speed, temperature), which can mask or mimic damage signatures [19]. Finally, detecting and localizing damage in large composite blades is difficult because global vibration modes lack spatial resolution, making it challenging to pinpoint the damage site without sensor-heavy setup or complementary techniques [20]. Acoustic emission (AE) can detect early damage in composite WTBs, but its use is limited by strong sensitivity to ambient noise and by wave attenuation in long blades, which complicates reliable and agile damage localization in many cases. These issues often necessitate dense sensor layouts and advanced filtering techniques [18], [19]. Iinfrared and thermographic methods are effective for detecting near-surface flaws but require sufficient thermal contrast and line-of-sight access [18]. While fibre-optic sensing offers excellent accuracy and distributed sensing capability, it can be costly and requires extensive installation, particularly in large blades [20]. Furthermore, drone-based imaging has recently grown in use for SHM of WTBs; however, it often faces real-world challenges such as sensitivity to environmental conditions, limited resolution, and regulatory constraints, which affect data quality and consistency [21], [22].

In comparison to the above-mentioned non-destructive inspection and condition monitoring methods, GW-based structural health monitoring (SHM) has gained popularity for composite WTBs. In favour of high frequency ultrasound waves, the GW technique can efficiently cover large portions of structures in a relatively short time using relatively few transducers, while also enabling in-depth detection. This capability makes the method highly effective for early identification and characterization of hidden structural anomalies, not accessible to visual or thermal inspection [23], [24], [25]. GW techniques demonstrated promise for all SHM levels - namely: detecting, localizing, quantifying, and classifying damage, and ultimately, assessing structural integrity [26]. Some studies showed that GW based SHM methods could accurately detect hidden defects in complex composites with multiple layers [27], [28], [29]. Such linear and nonlinear techniques can be exploited for highly sensitive, long-range monitoring of insignificant discontinuities in different layers [30], [31], [32], [33]. Typically, a network of low-cost and lightweight broadband transducers e.g., piezoelectric lead zirconium titanate transducers (PZTs) are mounted on the surface of blades [29].

Two GW techniques namely non-linear acoustics and a ‘pitch-catch’ method was exploited by Yang et al. [34] to investigate wave behaviour in small-scale turbine blades. Their research resulted in successful detection and localisation of impact damage. Shoja et al. [35] further developed GW techniques to employ an icing index for detecting ice formation on blades. Another research [36] used phase velocity variations to defect identification and sizing with high accuracy. Nevertheless, GW Nevertheless, GW techniques also face limitations. Wave propagation in anisotropic, multi-curvature composites such as WTBs is sometimes dispersive and attenuative, complicating signal interpretation and damage localization. Environmental and operational variability can add further uncertainty, and significant computational resources are often required for advanced signal processing [19], [36].

As a solution to these challenges, the analysis of structural data using machine learning (ML) algorithms has been increasingly utilized for autonomous condition monitoring of composite structures, including WTBs. Humer et al. [23] applied a deep neural network (DNN) to extend a wave damage interaction coefficients (WDICs) database for damage identification, correlating the generated GW data and potential damage characteristics of plate-like structures. Kundu et al. [37] generalised an ML-based method for AE damage localisation and characterisation on a carbon fibre composite panel under variable loading. Some researchers have utilized innovative ML-based methods to improve wind turbine health monitoring. Oliveira et al. [14] proposed an NDT framework for WTB damage identification through a ‘novelty detection’ algorithm, where they employed the discrete Fourier transform (DFT) and principal component analysis (PCA) for feature extraction from ultrasound signals after denoising them using the discrete wavelet transform (DWT). Movsessian et al. [38] suggested a two-layer artificial neural network (ANN) regression model for a vibration-based SHM system to detect wind turbine damage during operation.

Many recent works have presented ML-based SHM methods to autonomously assess damage in laminated composites. These evolving approaches blend ML architectures with established methods- e.g., GW-based techniques. Powerful prediction algorithms can be developed by data-driven ML models, bypassing the need for explicit implementation of pre-established solutions [39], [40], [41]. As a case in point, Junqueira et al. [42] presented a two-stage Digital Twin (DT) based on a deep learning (DL) framework, narrowing the difference between GW signals recorded during simulation and experiment (low-and high-fidelity data, respectively), and subsequently producing considerably ‘close-to-experiment’ signals. Such approaches will enhance SHM outcome, especially in situations where reliable experimental or on-site data is limited. In this regard, ‘detection probability’ charts can also be generated to investigate the reliability of SHM systems. Cappugi et al. [43] suggested an ML model to estimate wind turbine power loss caused by erosion on the blades’ edge. A large dataset was generated using computational fluid dynamics (CFD) model for a lab-sized wind turbine, validated by some experiments.

To boost traditional methods, a variety of recent studies employed ML-based frameworks to detect and/or categorise damage type or severity. A new study [44] merged the phased array guided wave (PAGW) technique and finite element (FE) modelling with DL to quantitatively evaluate damage in cracked curved plate structures and yielded better results relative to traditional curve-fitting approaches. Wu et al. [45] exploited an inverse Bayesian process based on a GW interaction model to identify damage across an infinite plate. Another work [46] analysed Lamb waves in composite blades via a Bayesian algorithm, with a focus on enhancing sensor arrays. Xue et al. [47] introduced a multi-task Bayesian learning model to localise damage using data collected from a small set of sensors. Also, a convolutional neural network (CNN) blended with 'Large Eddy' simulation was exploited in a recent study [48] to predict wake and generated power associated with an offshore wind turbine. Another ML model was employed to detect icing on wind turbine rotors and the associated power loss, wherein data from a large network of sensors were combined with physical data to enhance the output [49].

Recent publications indicate that there remains significant potential to establish intelligent SHM frameworks for composite blades, interpreting adequate GW data from various damage conditions through a tailored ML architecture. Larger response datasets usually pave the way for a more effective ML algorithm, capable of more accurate damage detection and classification. There are, however, limitations for accumulating large amount of reliable data through only experiments. It is not viable to conduct numerous standardised tests under fully controlled conditions in both research and industrial settings. Variability in ambient conditions and the human error can lead to inconsistencies, with repeated laboratory tests often yielding slightly varying, or in some cases yield significantly divergent results. Therefore, it is critical to generate sufficient data through validated numerical simulations. This offers a controlled and repeatable means to complement the experimental results.

This paper proposes a custom-designed, data-driven SHM system for composite WTBs, which is achieved through collecting and classifying a large GW dataset from experiments and numerical simulations. First, limited GW response data were collected through laboratory tests on healthy and damaged composite WTBs. Next, FE models were developed in Abaqus/CAE, defining multiple sensing points, instead of using a small set. After verifying the FE simulations using experimental GW signals, both experimental and simulated signals were converted to red, green, and blue (RGB) scalograms, to be imported into a ML model. The hybrid ML architecture is specifically designed to distinguish between damaged and undamaged blades, as well as to categorise the type of damage. Key stages of the proposed work are illustrated in *Fig 1.*

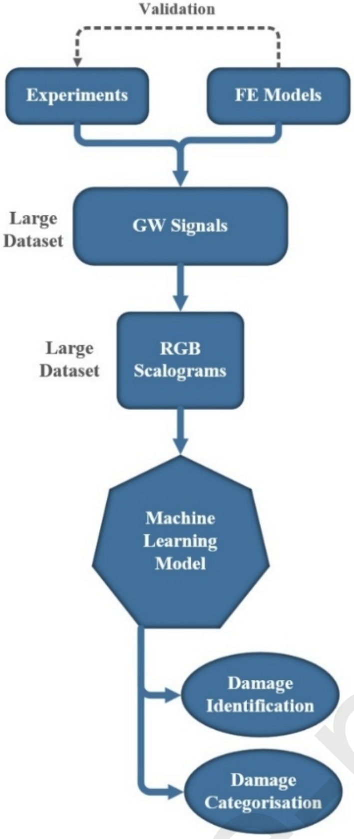

Fig 1. *Flowchart of damage identification and categorisation.*

2. Experimental investigation

The propagation behaviour observed in composite specimens is governed by dispersion, anisotropy and frequency-dependent attenuation introduced by the laminate architecture and fibre orientations, so mode shapes, phase/group velocities and energy partitioning must be characterized for the specific lay-up and frequency band used [50]. Experimental work on composite panels and scaled blades shows that interactions between GWs and damage produce reflections, scattering and mode conversions whose signatures (time-of-flight shifts, amplitude reductions or new arrivals) are the primary observables exploited for detection and localisation in the lab [51]. Importantly for WTB specimens, geometric effects of blades like local curvature, ply-by-ply lay-up, thickness variation and boundary conditions can significantly alter amplitudes and arrival times compared with flat, isotropic plate baselines, so these factors are routinely included in laboratory test designs and interpretation [52]. Finally, the choice and mounting of PZT actuators/sensors (type, bonding method and relative placement) strongly affects which modes are excited and the signal clarity recorded in lab tests and therefore must be described and controlled when validating finite-element models or comparing experimental cases [53]. Building on the mentioned principles, different PZT transducers were examined in several locations across the blade samples, ensuring the best resolution of the captured signals using an appropriate excitation frequency. Consequently, the setup configuration and experimental procedure are proposed as follows. Actuation-induced GW propagation signals were recorded during a set of laboratory experiments on scaled down blade samples.

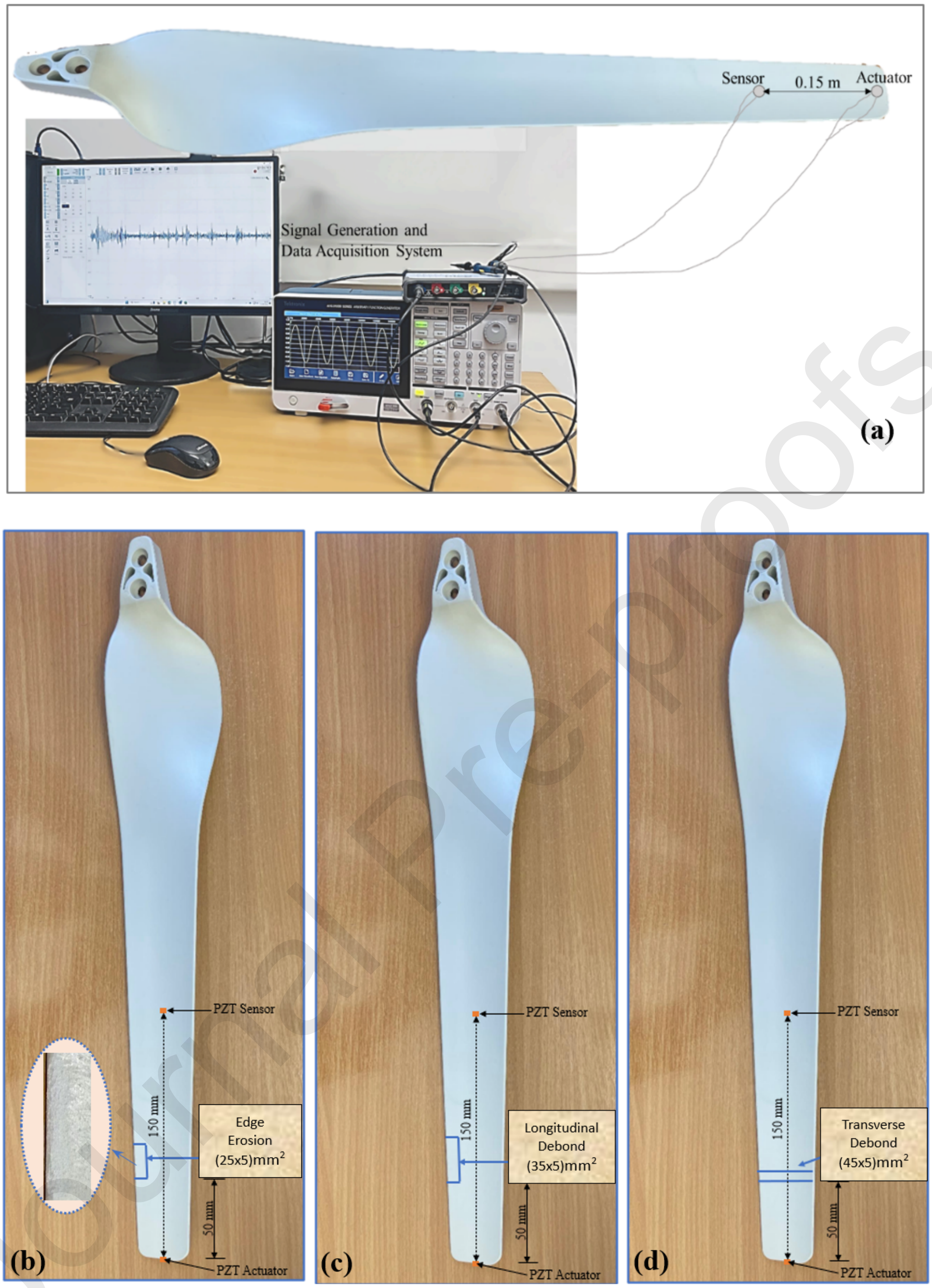

Fig 2. *(a) Experimental setup for GW-based inspection of WTB samples, and depiction of WTBs for: (b) erosion damage (c) longitudinal debonding (d) transverse debonding.*

The collected data were subsequently exploited to verify the FE models described in Section 3. For actuation and reception of GW signals, circular PZTs with a diameter of 8 mm and a thickness of 0.5 mm were attached to the surfaces of both undamaged and damaged composite WTB samples using superglue. The sensor network was operated via a signal generator and data acquisition system. Four scaled-down WTB samples were considered for experimental study: one healthy blade (H), and three blades with erosion damage (ED), longitudinal debonding (LD), and transverse debonding (TD). A damage size of 25mm × 5mm was considered on the surface of each damaged case. All blades were

500 mm long and made of a glass fibre reinforced composite (GFRC) laminate (0^{o}/90^{o}/45^{o}/-45^{o}/90^{o}/0^{o}). Fig 2 presents the experimental setup and schematic depiction of blades under three damage scenarios. All experimental analyses were conducted using 5-cycle Hanning windowed sine burst signals at a frequency of 150 kHz, as the excitation for the PZT sensors. The actuation signal is shown in Fig 3 in both time and frequency domains.

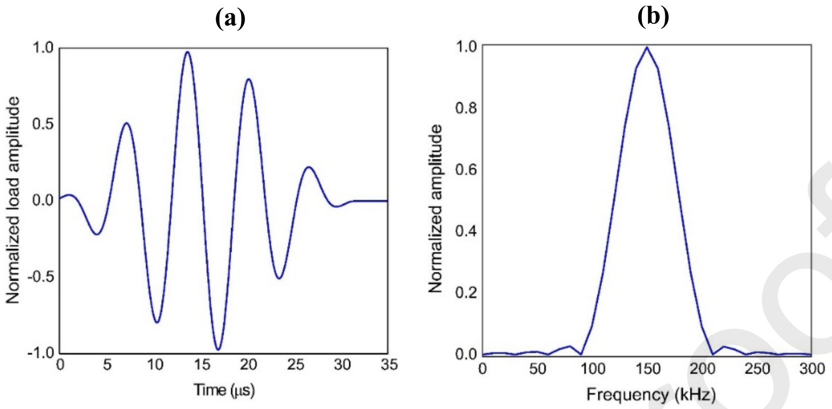

Fig 3. *Five-cycle sine actuation signal in a Hanning window at 150 kHz (a) in temporal domain, and (b) its frequency domain.*

In guided wave experiments, noise may arise from several sources, including electrical interference from the instrumentation, ambient vibrations or acoustic disturbances in the laboratory, boundary reflections at the specimen edges, and local variations within the composite material. To minimise these effects, a 5-cycle sine-Hanning pulse centred at 150 kHz was employed, which confined the excitation to a narrow frequency band and reduced unwanted reflections. Signals were further stabilised through averaging during acquisition, which suppressed random electronic noise.

3. Finite element analysis

To accurately simulate the healthy and damaged blades, three-dimensional (3D) finite element (FE) models were developed using Abaqus/CAE Academic Edition 2022. These models are verified by experimental GW signals detailed in Section 2.

3.1. Damage initiation and evolution criteria

The failure behaviour of composite materials is commonly modelled in two stages: damage initiation and damage evolution, as per the progressive failure theory. In this work, Hashin's failure criteria are adopted for predicting damage initiation in fibre-reinforced composites [50].

Hashin's criteria categorize failure into four distinct modes: fibre tension, fibre compression, matrix tension, and matrix compression. Each mode is governed by a separate initiation equation involving the components of the effective stress tensor and relevant strength parameters of the material. The criteria also incorporate the influence of shear stress through a coefficient that modulates its contribution, particularly for the fibre tension and matrix modes [50] [51]. The effective stress, $\hat{\sigma}$, is derived from the nominal stress, σ, using a damage operator, M, such that:

$$\hat{\sigma} = (1)$$

The damage operator modifies the stress response based on the internal damage variables corresponding to fibre damage (d_f), matrix damage (d_m) and shear damage (d_s). Initially, in the absence of any damage, the operator is the identity matrix, indicating purely elastic behaviour. Once damage initiates in any mode, the operator introduces reductions in the effective stress that propagate through the structure and influence further damage initiation and progression.

Following initiation, damage evolution governs the degradation of material stiffness as damage propagates. This evolution is represented through a damage-modified elasticity matrix $\boldsymbol{C_d}$, which accounts for the loss of stiffness in the fibre, matrix, and shear directions. The material stiffness response (σ) is then computed as:

$$\sigma = \boldsymbol{C_d}(2)$$

where ε is the strain tensor [50].

The evolution of damage is modelled using equivalent stress–displacement relations specific to each failure mode. These are defined using the Macauley bracket operator to distinguish between tension and compression. The equivalent displacement δ_{eq}increases from an initial value δ_{eq}^0 at damage onset to a critical value δ_{eq}^f at complete failure. The damage variable d for each mode evolves linearly according to:

$$d = \frac{\delta_{eq}^f\left(\delta_{eq} - \delta_{eq}^0\right)}{\delta_{eq}\left(\delta_{eq}^f - \delta_{eq}^0\right)}(3)$$

The critical equivalent displacement δ_{eq}^f is determined from the fracture energy (G_c), representing the area under the stress–displacement curve, assuming a linear softening law [50] [51].

The entire damage initiation and evolution framework, including Hashin's criteria and stiffness degradation, has been implemented in Abaqus/CAE through the material properties relevant to damage initiation and evolution of the GFRC blades [52], as presented in *Table 1*.

Table 1. *Material properties for damaged regions as per Hashin's criteria.*

Property	Value
Tensile strength - fibre direction (GPa)	1.0123
Compressive strength - fibre direction (GPa)	0.978
Tensile strength - perpendicular to the fibre direction (GPa)	0.0295
Compressive strength - perpendicular to the fibre direction (GPa)	0.1718
Longitudinal shear strength (GPa)	0.0353

Transverse shear strength (GPa)	0.0353
Fracture energy for fibre tension (N/m)	300
Fracture energy for fibre compression (N/m)	300
Fracture energy for matrix tension (N/m)	600
Fracture energy for matrix compression (N/m)	600

3.2. Simulation

A set of FE simulations were run to produce a large, reliable dataset for one undamaged and three damaged blades namely: healthy (H), erosion damage (ED), longitudinal debonding (LD), and transverse debonding (TD). Similar to laboratory experiments in Section 2, all modelled blades were considered to be made of GFRC, with the same dimensions 500 mm long and 3 mm thick. *Table 2* provides an overview of the cases analysed. The elastic material properties used for undamaged regions of all blades are given in *Table 3*, where the subscripts 1, 2, and 3 correspond to the longitudinal, transverse, and thickness directions of the blades, respectively.

The HASHIN criteria is used to model progressive damage failure models. The model works well where the overall damage information is sufficient [53].[54] It was also observed that the comparison of experimental and numerical simulations demonstrated a high level of agreement in terms of the global deformation [53][54]. PUCK failure criteria are used to obtain a detailed analysis to understand damage occurrence in individual constituents. Although PUCK failure criteria is a better predictor of the distribution of failure than the HASHIN criteria [54]; the present model incorporates cohesive zone modelling (CZM) and HASHIN criteria to model erosion damage, longitudinal debond and transverse debond.

The wind turbine blade (WTB) is modeled using an elliptical cross-section that is extruded to a depth, serving as the reference section. Subsequent sections along the blade length are created by extending this cross-section using datum planes positioned longitudinally along the blade. The curved sections are provided using spline in the sketch module. These cross-sections are then connected through solid extrusion in the Part module. The datum planes are aligned to correspond with the WTB length used in the experimental study. After suitable partitioning to facilitate proper meshing, the solid WTB model is converted into a shell model. Material properties are assigned through the shell composite section, with inputs specifying the thickness and orientation angle of each ply. The elastic material properties used for the WTB are given in Table 3 and the orientation angles for each ply are detailed in Section 2 of the manuscript. The WTBs are modelled using four-node doubly curved S4R elements, each measuring 0.5 mm × 0.5 mm, featuring hourglass control and reduced integration.

In the 3-mm thick composite blade laminate, multiple zero-volume damage regions were introduced to replicate damage sizes detailed in *Table 2*. The node-to-node connections within the targeted elements were removed to precisely model the damage scenarios. Damage modelling is carried out without the use of cohesive elements. The elastic properties of the damaged elements are scaled by a factor corresponding to their thickness. For both longitudinal and transverse debonding, this scaling factor is taken as 0.0132 mm, with the corresponding modulus of elasticity and shear modulus in both directions specified as 850 MPa [55]. To replicate the effect of cohesive behaviour without explicitly including cohesive elements, the modulus values are upscaled based on the thickness factor. For the erosion damage model, a thickness of 1×10^{-6} mm is used to model damage, and the modulus value are upscaled based on this factor. A surface-based traction separation approach is used. Connector damage mechanisms are defined using force-based damage initiation and a tabular form of motion-based damage evolution [55].

Table 2. *Specifications of simulated damaged cases.*

Case	Status	Damage size		Damage distance from the blade tip (mm)
		Length (mm)	Width (mm)	
H	Healthy	---	---	---
ED	Erosion damage	15 25 35	5	50
LD	Longitudinal debonding	15 25 35	5	50
TD	Transverse debonding	15 25 35	5	50

Table 3. *Elastic material properties of the GFRC blades[56].*

Property		Value
Young’s modulus (GPa)	E_{11}	41
	E_{22}	9
	E_{33}	9
Shear modulus (GPa)	G_{12}	4.1
	G_{13}	4.1

	G_{23}	4.1
Poisson's ratio	ν_{12}	0.27
	ν_{13}	0.27
	ν_{23}	0.27
Density (kg/m^3)	ρ	1890

In addition to the actuation load very close to the tip of the blades, three linear arrays of sensing points were defined on their top surface, providing about 50 sensing positions for each blade to produce sufficient GW response data. Applying the same actuation pulse of 150 kHz detailed in Section 2, the simulations were run once for the healthy case as the reference state, and three times for each damaged case, considering the damage sizes specified in *Table 2*. In other words, one healthy and nine damaged blades were modelled, and FE simulations were run for each case. A typical layout is represented in *Fig 4*.

Considering fixed boundary condition at the root of the blades similar to the experimental study, all simulations were conducted in Dynamic Explicit mode with a time step of 0.1 microseconds and were run for a total duration of 500 microseconds to ensure comprehensive analysis of the dynamic response. The FE model of the WTB replicating the experimental conditions prepared in Abaqus/CAE is shown in *Fig 5*.

The short propagation path between actuator and sensors (approximately 125-175 mm for 3 mm-thick blade samples), as shown in *Fig. 4* resulted in a high signal-to-noise ratio, thereby confirming that influence of noise in experimental work was negligible.

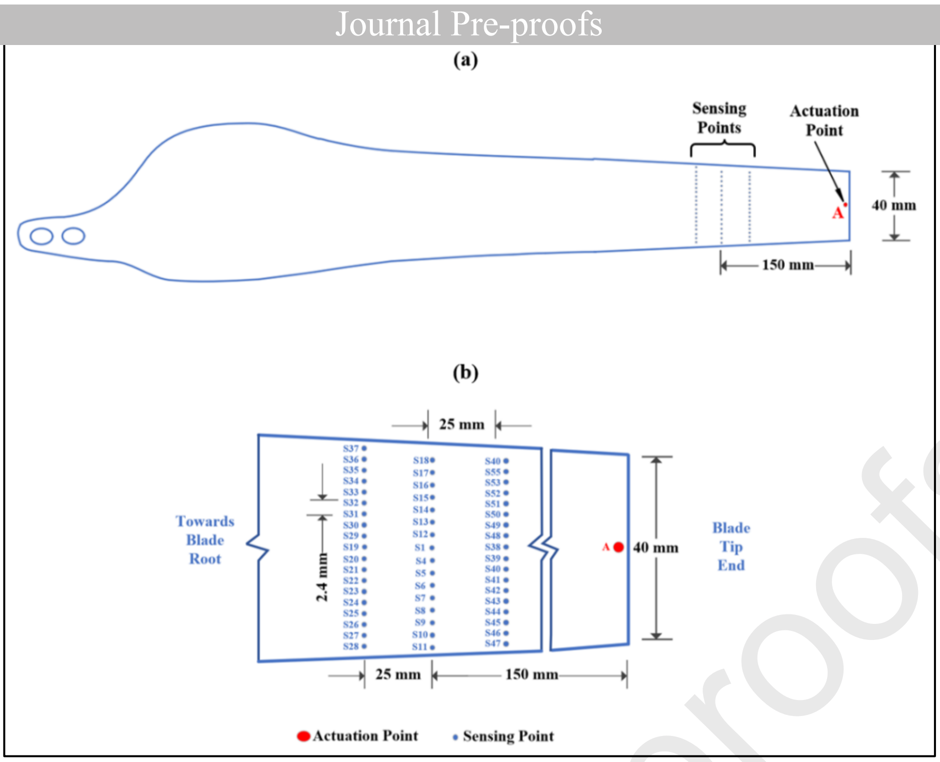

Fig 4. *(a) Overall configuration of the simulated actuation-sensing location on a sample blade, (b) the detailed view of the sensing points.*

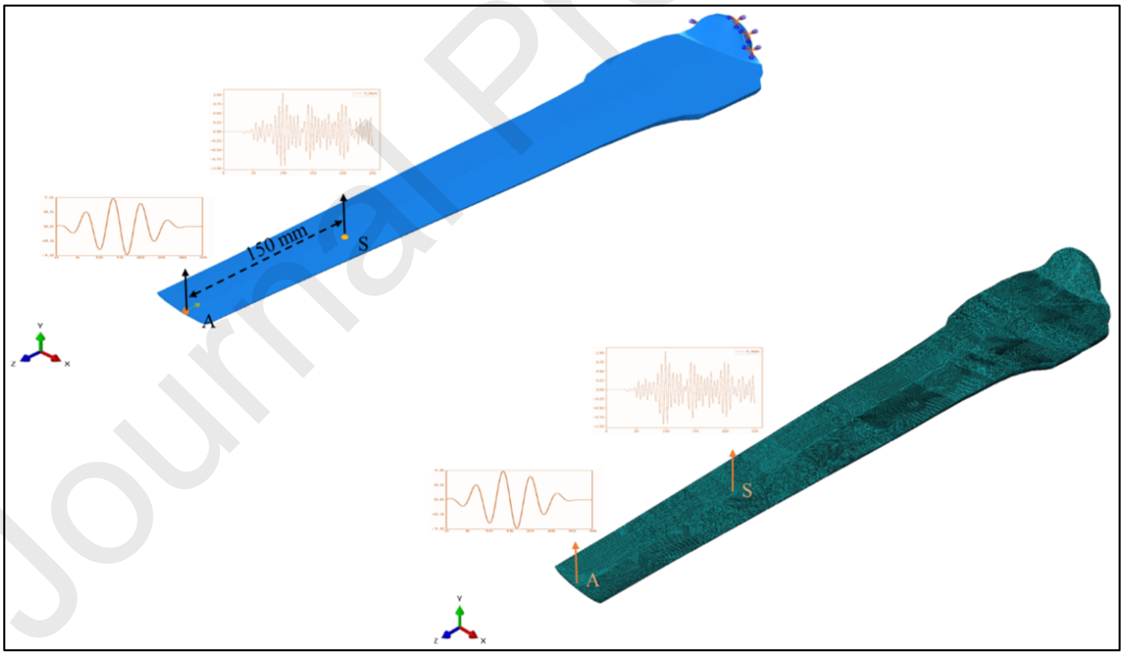

Fig 5. *FE model of the WTB showing load as wave actuation, boundary conditions and mesh for simulating GW propagation under different conditions (A: actuation point; S: sensing locations).*

4. Machine learning-based autonomous health monitoring of wind turbine blades

4.1. Data processing

During experiments and simulations, raw GW signals were recorded at the sensing points, stored as out-of-the-plane deformation over time. Dividing by their maximum absolute amplitude, these signals were normalised to have values between -1 and +1. To better analyse their frequency content, all signals were then converted into uniform RGB scalograms via a Continuous Wavelet Transform (CWT).

Unlike the limited number of sensors used in experiments, more than 50 sensing points are introduced in each of the ten simulations detailed in Section 3 (~54-57 points depending on the case). This allowed for above 50 displacement-time signals per model. Afterwards, five CWT scalograms were produced from each experimental and numerical signal using a MATLAB script, varying bandwidths and centre frequencies of the wavelet function (representing images with different time and frequency resolutions). Overall, above 2500 scalograms are produced for each blade condition and only 2000 scalogram per case were randomly selected to be used in the ML block. This size of dataset across different cases (H, ED, LD & TD) allowed for rigorously training, validating, and testing the damage identification and classification tasks, thereby reducing the risk of overfitting and enhancing the robustness of the evaluation. In summary, a combination of experimental and numerical GW data was processed to be fed into the tailored ML architecture.

The total dataset consisted of 2,000 samples (500 per class: H, ED, LD, TD), obtained from both experimental and numerical studies. Following the standard practice in machine learning, 80% of the data (1,600 samples) were randomly assigned for training and validation, while the remaining 20% (400 samples) were reserved exclusively for testing model performance. Thus, the testing data reported in *Table 4* refers to this 20% subset.

The process of random data splitting was repeated ten times, and the averaged performance across folds was reported using confusion matrices and confidence intervals, explained in Section 5. This procedure ensures robustness and avoids bias linked to a particular train–test partition.

2000 RGB scalograms per case with dimensions of 233×175 pixels at 40 dots per inch (dpi) were generated, visualising the spectral content of captured signals over time (the time-frequency domain). Converting one-dimensional time data into two-dimensional scalograms has provided a depiction of the signals' energy density, revealing more damage characteristics. The hybrid ML model was fed with the described scalograms in the form of numerical arrays, while slicing these input data into three subsets training, validation, and testing. For each class, 1600 images (80%) were used for the training-validation phase, and 400 images (20%) were reserved for testing the ML model; see

Table **4**.

After being resized to 233×175 pixels, each RGB image was normalised by adjusting pixel values to fall within the [0,1] range:

$$I_N = \frac{I_O}{255} (4)$$

where, I_N and I_O are normalised and original image pixel value, respectively.

***Table 4**. Datasets for machine learning.*

Class	Total Count	Training-Validation	Testing

			#	%	#	%
H	Healthy	2000	1600	80%	400	20%
ED	Erosion damage	2000	1600	80%	400	20%
LD	Longitudinal debonding	2000	1600	80%	400	20%
TD	Transverse debonding	2000	1600	80%	400	20%
	Sum	8000	6400	80%	1600	20%

4.2. Machine learning model

For better outcome, a transfer learning (TL)-based model has been developed in this study, enabling RGB image classification for four categories of composite blades, as outlined in *Table 5*. This approach allowed for health status monitoring of blades, with remarkable accuracy and agility.

Transfer learning (TL) was selected because it allows to exploit pre-trained feature extraction capabilities from large-scale image datasets, thereby reducing training time and data requirements. In this study, scalogram images generated from guided wave signals were used as inputs, and the VGG16 backbone was adapted through TL to capture discriminative time-frequency features. This approach significantly enhanced classification performance compared to training a model from scratch, especially given the limited size of experimental datasets.

A ML-model based on the VGG16 architecture, a deep convolutional neural network (DCNN), was developed to reduce the dependence on large, labelled datasets and high computational power for image classification. This DCNN architecture uses 16 customised convolutional layers with pre-training and proved to be powerful for pattern recognition in large visual datasets [57]. The 16 layers include five stages of hybrid convolution, often followed by three Fully Connected (Dense) layers, and one Softmax classifier [58] at the end. In this paper, the three Dense layers were replaced with a Global Average Pooling (GAP) layer for higher effectiveness [59], [60]. In addition to the Categorical Cross-Entropy Loss as loss function [61], the proposed model is equipped with an ADAM (Adaptive Moment Estimation) Optimiser [62] for better convolution in the training phase. Overall, the introduced model can effectively extract visual features through applying hierarchical spatial patterns e.g., edges and complex textures in composite structures. A visual summary of data acquisition, processing and classification in this study is shown in *Fig 6*.

***Table 5**. Blade condition classes.*

Class	Condition	Remarks
Class I	Healthy	No structural damage

	(H)	
Class II	Erosion Damage (ED)	Leading edge erosion on the top surface of the blade
Class III	Longitudinal Debonding (LD)	Partial layer separation along the length of the blade, on the top surface
Class IV	Transverse Debonding (TD)	Partial layer separation across the width of the blade, on the top surface

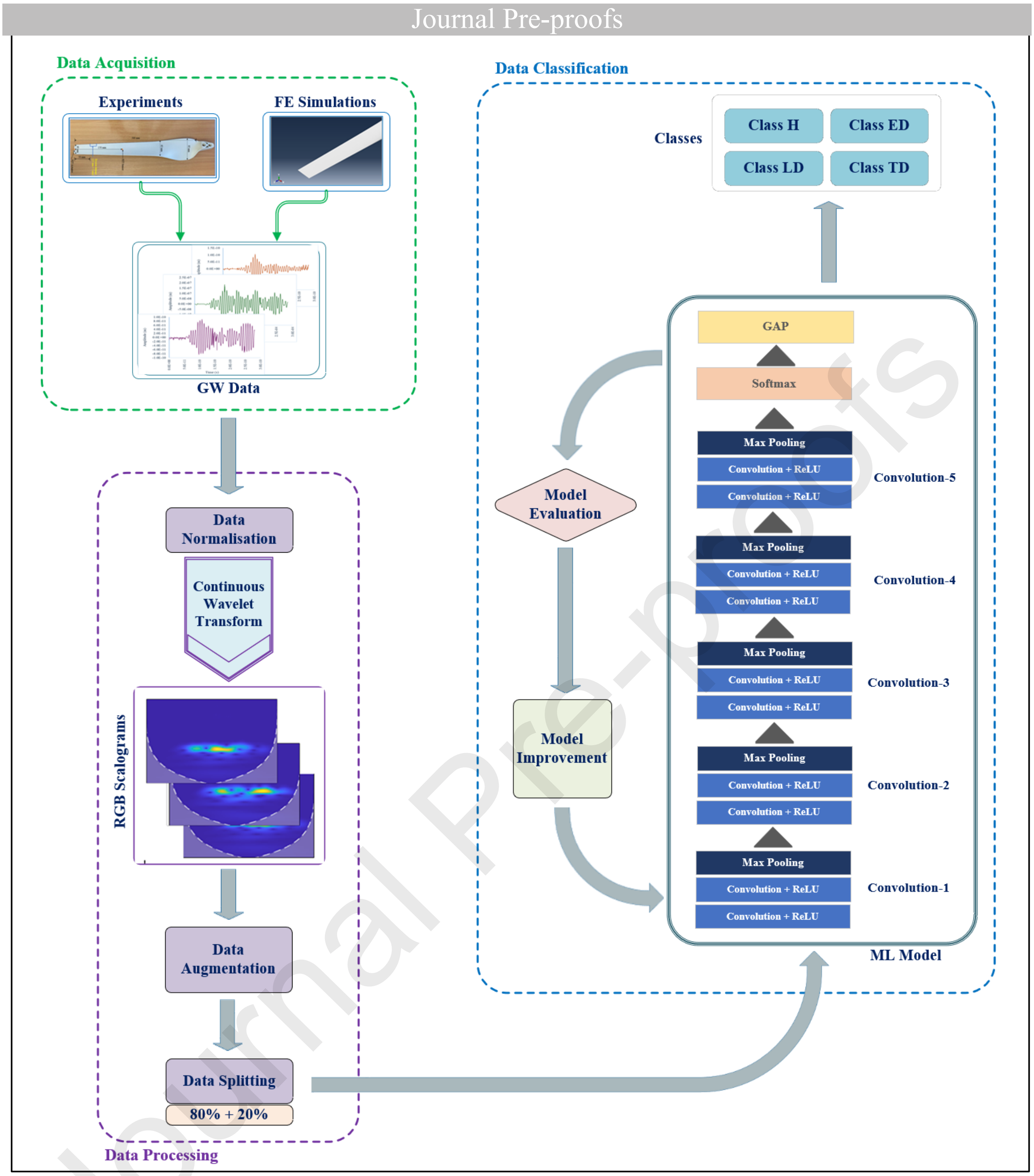

***Fig 6.** Workflow of WTB damage identification/classification using the VGG16-based architecture.*

Main blocks in the in the proposed architecture are described in the following:

i) Feature extraction: Hybrid convolutional layers extract image characteristics by computing feature maps [63] as below:

$$M_{i,j}^{l} = f\left(\sum_{m.n} W_{m,n}^{l}.M_{(i+m),(j+n)}^{l-1} + B^{l}\right)(5)$$

where, $M_{i,j}^{l}$ is the output feature map at layer l, $W_{m,n}^{l}$ are the kernel weights, $M_{(i+m),(j+n)}^{l-1}$ are the feature values from the previous layer, B^{l} is the bias of layer l, and $f(.)$ denotes the Rectified Linear Unit (ReLU) Activation Function [63], which is defined as:

$$f(x) = \max(0,x) (6)$$

ii) Global Average Pooling (GAP) layer: In lieu of three Fully Connected layers commonly used in VGG16, a GAP layer is utilised in this work, reducing the number of parameters in the model to mitigate overfitting. The GAP is defined as:

$$GAP = \frac{1}{N}\sum_{i=1}^{N} M_i (7)$$

where, N is the number of feature maps, and M_i is the *i-th* feature map.

iii) Softmax classifier: To classify images into four categories, a Softmax classifier is added, as the final layer:

$$P_i = \frac{e^{z_i}}{\sum_{j=1}^{4} e^{z_j}} (8)$$

where, P_i is the predicted probability of class i, e represents Euler's number, and z_i is the raw output from the last dense layer.

iv) Loss function: The Categorical Cross-Entropy Loss ($CCEL$) is applied for the four classes:

$$CCEL = -\sum_{i=1}^{4} y_i \operatorname{Ln}(P_i) (9)$$

where, y_i is the true label (one-hot encoded) of class i, Ln denotes the natural logarithm, and P_i is the predicted probability of class i. The latter comes from the Softmax Function described as Equation 8 above and gives the probability that the model assigns to each class.

v) ADAM optimiser: At the training stage, this optimiser helps to consistently update the weights of neural network layers. It can be formulated as follows:

$$\alpha_{t+1} = \alpha_t - r\frac{m_I}{\sqrt{m_{II}} + c} (10)$$

where, α_{t+1} is the updated weight at the next time step, α_t is the current weight, r is the learning rate, m_I and m_{II} are the first and second Moment Estimate, and c is a small constant.

4.3. Model performance evaluation

The metrics described below are employed to assess the performance of the proposed ML model. Relevant results will be reported in Section 5.

Accuracy Percentage: The model's accuracy for each class is calculated as below:

$$AC\% = \frac{N_{CP}}{N_{TP}} \times 100 \ (11)$$

where, $AC\%$ denotes accuracy percentage, N_{CP} is the number of correct predictions, and N_{TP} is the total number of predictions.

Confusion Matrix: To assess how effectively the model can perform the classification task, a Confusion Matrix, $\boldsymbol{C}$, is generated:

$$\boldsymbol{C} = [c_{ij}] \ (12)$$

where, each c_{ij} element denotes the number of times an instance of true class i was predicted as class j [64]. The indicators i and j both range from 1 to 4, showing the four classes considered in this study. This square matrix compares the model's predicted labels with the actual labels, showing how many predictions were correct or incorrect (True or False Labels).

Confidence Interval: To predict and quantify the uncertainty of the ML model within known and newly introduced data, a Random Forest model is employed, wherein each tree generates an individual prediction, and the overall prediction is the mean of all trees in the ensemble. The objective is to investigate how accurate the model could extrapolate beyond observed values. Uncertainty is quantified by calculating the standard deviation of predictions from each tree, capturing the variability in the model's outputs. The Confidence Interval (CI) is defined as:

$$CI = \overline{Y} \pm 1.960 \times \mathrm{S} \ (13)$$

where, $\overline{Y}$ denotes the predicted mean, and S is the standard deviation, providing a 95% confidence interval under a normality assumption [64].

The datasets were divided into training/validation (80%) and testing (20%) subsets as detailed in Section 4.1 for clustering evaluation. Model performance was assessed using standard classification metrics, including accuracy, precision, recall, and F1-score as explained in this section.

5. Results and Discussions

Results obtained from the experimental study on WTBs (Section 2), numerical simulations of WTBs (Section 3) and the proposed ML model (Section 4) are presented and discussed in this section.

5.1. Autonomous health monitoring of composite blades using experimental signals

The time domain response collected from experiments on one healthy blade and three damaged blades, namely healthy, erosion damage, longitudinal debonding and transverse debonding are shown in *Fig 7*. Typical RGB images generated from the experimental time signals can be seen in *Fig 8* in the time-frequency domain. The confusion chart obtained from the 400 experimental data sets for the healthy and damaged states of WTBs is presented in *Fig 9.* The confidence intervals corresponding to healthy and damaged states are also reported in *Fig 10*.

The experiments and simulations in this study were conducted using a 5-cycle sine-Hanning pulse as excitation (Point A in *Fig. 4*), at a relatively high central frequency (150 kHz). Powerful circular PZT transducers allow for capturing high quality structural response, providing significant difference between experimental signals captured from healthy and different damaged samples. For numerical simulations, a sampling interval of 0.1 μs was applied (i.e., a sampling frequency of 10 MHz), which is around 33 times greater than the Nyquist–Shannon sampling frequency (2×150kHz=300kHz). Consequently, minimal attenuation was observed in experimental study and numerical simulations.

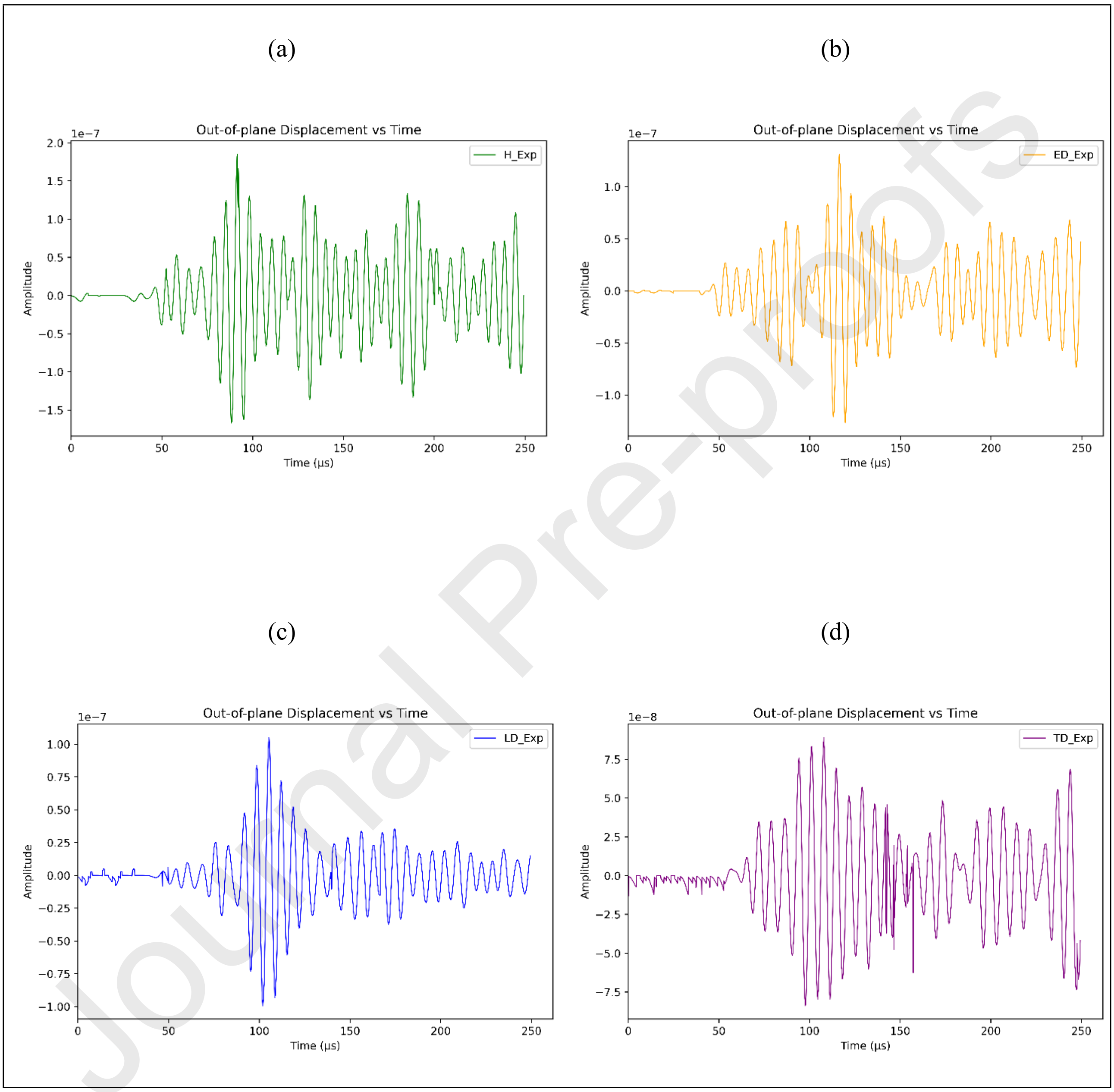

***Fig** 7. Experimental GW signals from one sensing point for:*
(a) healthy case (b) erosion damage (c) longitudinal debonding, and (d) transverse debonding.

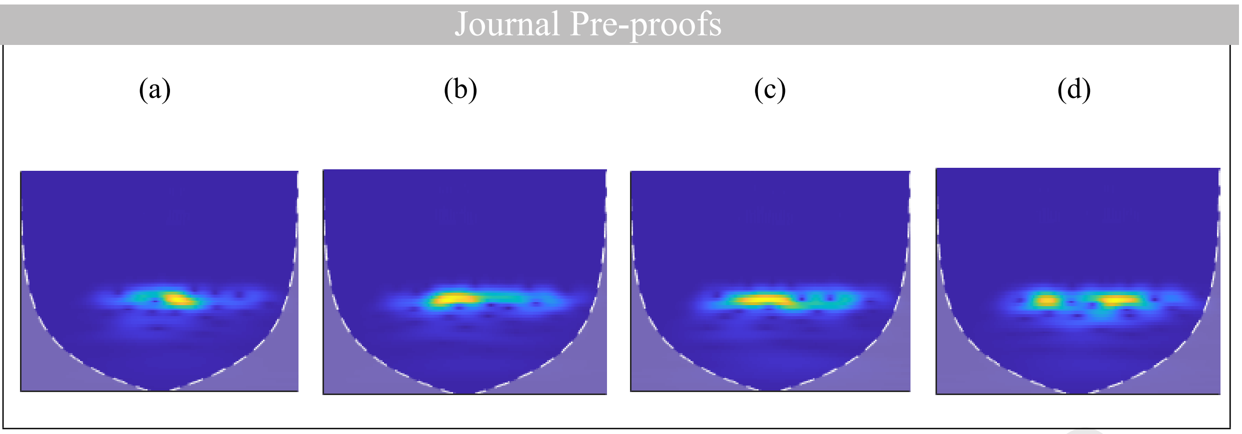

Fig 8*. Typical RGB scalograms of experimental signals for:*
(a) healthy blade, (b) erosion damage, (c) longitudinal debonding, and (d) transverse debonding.

It is observed that the presence of damage leads to a reduction in the amplitude of the response signals in symmetric and antisymmetric mode, compared to the healthy condition, as seen from *Figs 7(a)* to *7(d)*. This reduction is attributed to wave attenuation caused by the interaction of guided waves with the damage, resulting in increased energy absorption relative to the healthy WTB model. This can also be observed from *Figs 8(a)* to *8(d)*. It should be noted that scalograms are generated considering different time and frequency resolutions (i.e., varying bandwidths and centre frequencies for the wavelet function). As detailed in Section 4.1, they are produced for the classification task performed by the ML model; so, the different patterns associated with various damage signatures are not necessarily detectable by the human eye. Among the damage cases, transverse debonding showed increase scattered wave features. This indicates strong wave–damage interaction and anisotropic effects due to complex layered structure of the WTB.

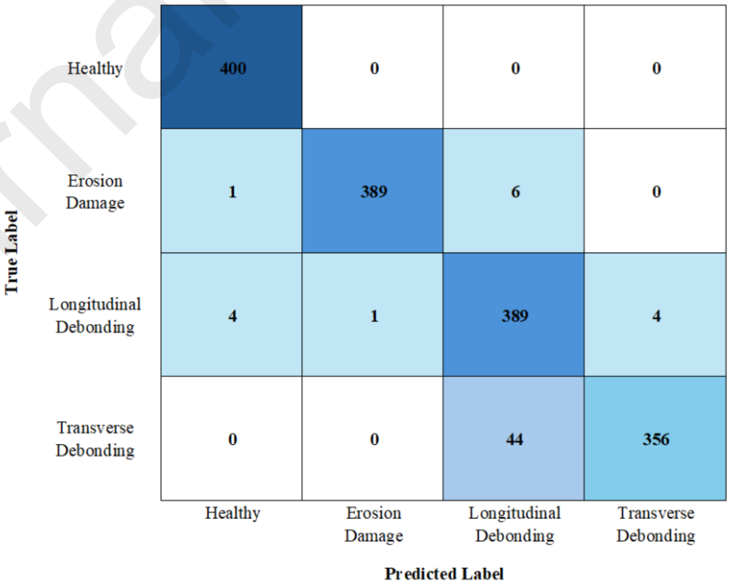

	Healthy	Erosion Damage	Longitudinal Debonding	Transverse Debonding
Healthy	400	0	0	0
Erosion Damage	1	389	6	0
Longitudinal Debonding	4	1	389	4
Transverse Debonding	0	0	44	356

Fig 9*. Testing performance of the TL model using the 400 experimental data/class.*

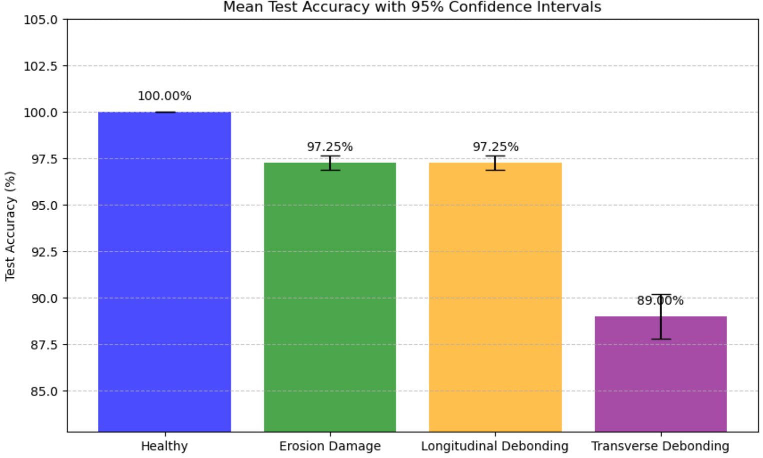

Fig 10. *Class-wise confidence intervals for predictions using 400 experimental data (average accuracy: 95.88%).*

An average classification accuracy of 95.88% was achieved by the ML model when predicting classes using experimental data, as illustrated in the confusion matrix shown in *Fig 9*. This highlights the effectiveness of the proposed approach in identifying damage based on experimental datasets. The confidence intervals (CIs) associated with each predicted class offer deeper insights into the model's predictive reliability when applied to experimental GW data, as presented in *Fig 10*.

The classification results in *Figs. 9* and *10*, derived from experimental data, indicate that the TL-based ML model performs consistently well across all predefined damage scenarios. For the healthy blade condition, the model attained perfect accuracy (100.00%), with all 400 test samples correctly classified, demonstrating robust detection of undamaged signals. In cases of erosion damage and longitudinal debonding, 389 out of 400 instances were correctly identified, corresponding to an accuracy of 97.25% for each scenario. These findings indicate the model’s strong capability in detecting subtle signal variations caused by surface wear and longitudinal delamination. However, in the case of transverse debonding, the accuracy decreased slightly to 89.00%, with 356 out of 400 samples accurately classified. This decline may be attributed to the increased complexity of wave scattering and mode conversion effects introduced by transverse defects, which pose greater challenges for model generalization.

Overall, the TL model achieved an average classification accuracy of approximately 96% using experimental GW data, demonstrating strong generalization ability and reliable performance in identifying various damage conditions in composite blades.

5.2. Autonomous health monitoring of composite blades using numerical signals

As elaborated in Section 3, FE simulations were conducted for one healthy WTB model and nine damaged models to develop the RGB scalograms and test the accuracy of the ML model for the numerical signals. In order to investigate GW propagation more effectively, the analysis primarily focused on the out-of-plane displacement that is, the displacement component perpendicular to the blade surface plotted as a function of propagation time. The response of the WTBs for healthy and damaged case acquired from numerical analysis is shown in *Fig 11*. The RGB scalograms obtained from these responses are presented in *Fig 12*.

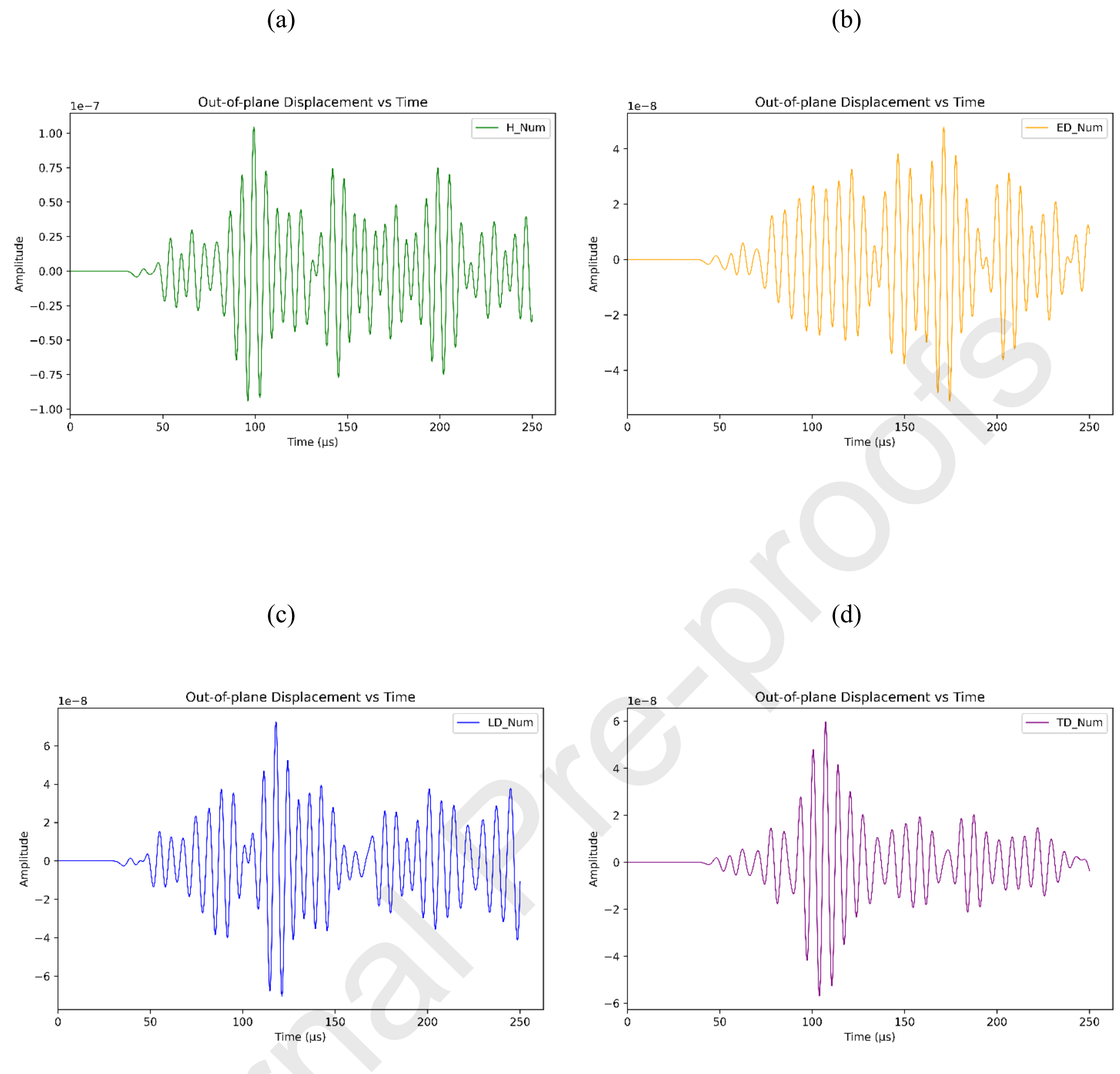

***Fig 11**. Simulated signals obtained from one sensing point corresponding to:*
(a) healthy blade, (b) erosion damage, (c) longitudinal debonding, and (d) transverse debonding.

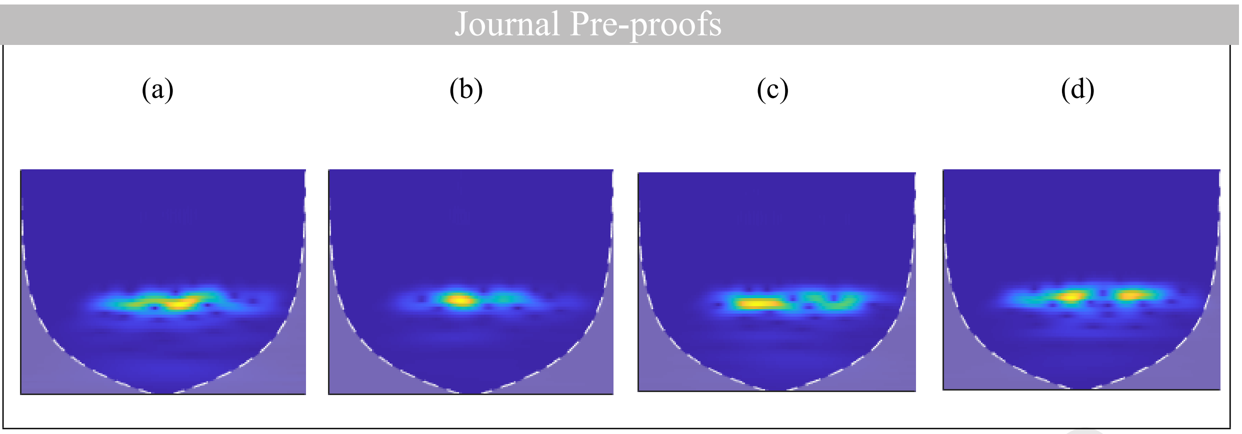

***Fig 12.** Typical RGB scalograms of FE-simulated signals for:*
(a) healthy blade, (b) erosion, (c) longitudinal debonding, and (d) transverse debonding.

Edge erosion damage (*Fig 11(b)*) decreased amplitude in comparison to healthy WTB *Fig 11(a)*). An approximately similar pattern can be seen in *Fig 11(c)* for longitudinal debonding and transverse debonding (*Fig 11*(*d*)).

It can be observed that the GW responses from experiments (*Fig 7*) and simulations (*Fig 11*) show a good level of agreement across all four conditions healthy blade, erosion damage, longitudinal debonding, and transverse debonding. The experimental and numerical signals exhibit close agreement in waveform behaviour, although amplitude differences remain due to the amplification ranges applied. To provide quantitative validation, the Spearman correlation coefficients are calculated between experimental and numerical signals for all cases: healthy (92.8%), erosion (93.41%), longitudinal debond (95.26%), and transverse debond (92.60%). These values confirm strong correspondence between experimental and simulated signals across healthy and damaged blade states. The close agreement between experimental and numerical results confirmed that the influence of noise in the experimental study was negligible.

For the healthy blade, both results show clean and symmetric waveforms with no major distortions. In the case of erosion damage, both signals show changes in waveform and amplitude compared to the healthy case. For longitudinal debonding, both synthetic and experiment display signal weakening and spreading. In the case of transverse debonding, both signals are clearly disrupted, with visible changes in amplitude and waveform symmetry. Overall, the experimental results support the trends observed in the simulations. It is also observed that the simulations accurately capture the main effects of each type of damage. This consistency confirms that FE-simulated data can be reliably used for training the ML model in to detect and classify damage.

The scalograms in *Fig 12* illustrate the time-frequency characteristics of GW signals obtained from FE simulations under different conditions of the WTBs. For the healthy blade (*Fig 12(a)*), the energy is moderately concentrated, indicating undisturbed GW propagation with minimal scattering or mode conversion. In contrast, the scalogram corresponding to the erosion case (*Fig 12(b)*) exhibits slightly scattered energy patterns, suggesting minor surface disruptions that lead to localized signal attenuation. More pronounced differences are observed in the debonding cases. The longitudinal debonding scenario (*Fig 12(c)*) shows a horizontally elongated energy pattern, indicative of wave interaction with an extended discontinuity along the fibre direction. The transverse debonding case (*Fig 12(d)*) displays a fragmented and laterally spread energy distribution, signifying substantial disruption in wave propagation due to the orthogonal nature of the defect relative to the fibre direction.

As mentioned before, it might be challenging for human eye to observe all the time-frequency domain information depicted in scalograms and compare different damage characteristics, but the tailored TL-based ML architecture can perform effective pattern recognition. However, a comparison between typical experimental (*Fig 8*) and simulated (*Fig 12*) scalograms reveals consistent trends in understanding the effect of different damage types on GW signal characteristics. In both sets of scalograms, the healthy blade condition (*a*) displays a well-defined, symmetric energy concentration in the time–frequency space, indicating smooth and undisturbed wave propagation. For erosion damage (*b*), both simulation and experiment show a slightly more energy pattern with lower intensity, suggesting minor scattering effects due to surface wear. The longitudinal debonding case (*c*) in both figures exhibits reduced signal intensity and increased spread in the scalogram. This pattern indicates energy loss and disruption due to delamination along the wave path, which is consistently captured in both the simulation and real test data. In the case of transverse debonding (*d*), the most complex wave interactions are observed. Both scalograms display more scattered and vertical features. The accuracy of the custom-designed ML architecture while being trained and validated through simulated data is illustrated in *Fig 13.* The confusion matrix presented in *Fig 14* depicts the predictive accuracy of the model across the four evaluated categories, considering the state of WTB. Similar to experimental results discussed in Section 5.1, the class-wise prediction accuracy of the TL model using simulation-driven data is presented in *Fig 15*, in the form of confidence intervals (CIs).

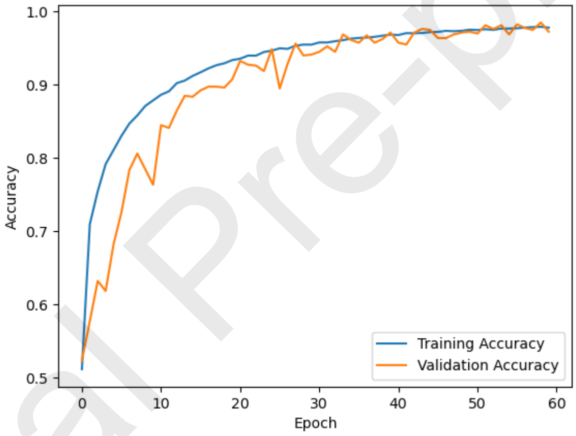

Fig 13. *Model accuracy for training and validation dataset.*

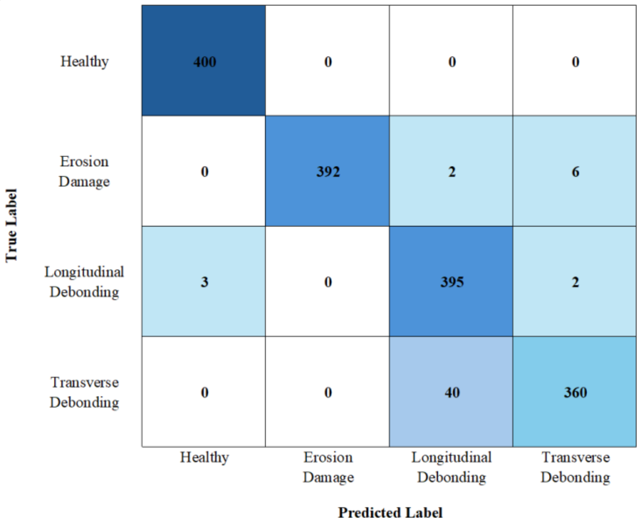

True Label \ Predicted Label	Healthy	Erosion Damage	Longitudinal Debonding	Transverse Debonding
Healthy	400	0	0	0
Erosion Damage	0	392	2	6
Longitudinal Debonding	3	0	395	2
Transverse Debonding	0	0	40	360

Fig 14*. Testing performance (10-fold average) of the TL model using the 400 simulated data.*

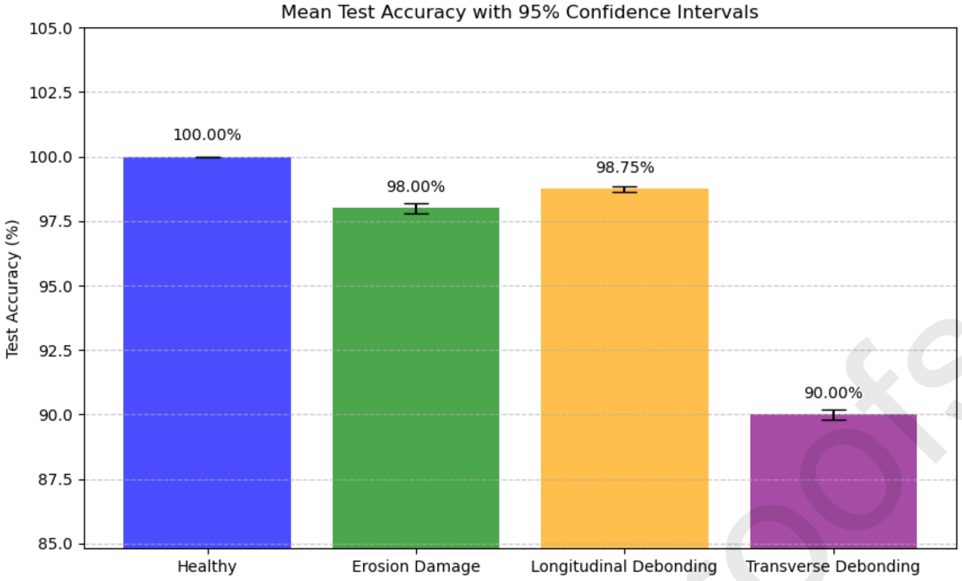

Fig 15. *10-fold average class-wise confidence intervals for predictions using 400 simulated data with a 10-fold average accuracy of 96.69%.*

A considerable accuracy of 97.82% is achieved for training and that for validation is 97.25%, as formulated in Section 4. These can be observed from *Fig 13*. The training and validation accuracy curves demonstrate the progressive improvement of the model's performance. Initially, the training accuracy rises sharply, followed by a gradual convergence with the validation accuracy. This convergence indicates that the model effectively generalizes to unseen data, with no significant signs of overfitting. The slight oscillations in the validation accuracy are within acceptable bounds and do not affect the overall stability of the model. These results affirm the robustness and predictive reliability of the trained model for classifying GW signal responses.

As described in Section 4.1, 400 data sets were used to test the TL-based model's accuracy. The classification performance of the model across the four damage conditions are observed from the confusion matrix depicted in *Fig 14*. The model achieved perfect classification (100.00% accuracy) for the healthy class, correctly identifying all 400 instances. For erosion damage and longitudinal debonding, the model exhibited high accuracy, with only minor misclassifications: 2 samples of erosion were confused with longitudinal debonding and 6 with transverse debonding, while 3 healthy and 2 transverse cases were misclassified as longitudinal debonding. The greatest confusion occurred between longitudinal and transverse debonding, with 40 transverse samples misclassified as longitudinal. Despite this, the model successfully classified 360 out of 400 transverse debonding cases correctly. Overall, the ML model shows strong performance across all classes, with minimal misclassification, particularly excelling in identifying healthy and longitudinally debonded blades. The average class-wise accuracy is remarkably 96.69%, which shows the effectiveness of this intelligent prediction work frame for identifying and classifying different damage scenarios using synthetic data.

The statistical metric shown in *Fig 15* contributes to a more transparent evaluation framework and supports the deployment of the model in real-world GW-based damage detection systems. This chart further underscores the strong predictive performance of the TL model when applied to simulated GW datasets. The model achieved perfect accuracy (100.00%) for the healthy blade class, reflecting its robustness in identifying undamaged states. Considerably high accuracy was also obtained for the erosion damage (98.00%) and longitudinal debonding (98.75%) classes, indicating the model's effectiveness in discerning these damage scenarios from one another. However, a notable reduction in classification accuracy was observed for the transverse debonding class (90.00%), suggesting a higher degree of confusion with other damage types particularly longitudinal debonding, as also evidenced in the confusion matrix (*Fig 14*).

This performance disparity may be attributed to the overlapping spatiotemporal and frequency characteristics of the GW signals generated by transverse and longitudinal debonding, which can challenge even advanced classification models. This demonstrates the high potential of TL-based models for automated damage classification in composite blades using GW response data. It is important to note that the impressive average accuracy of about 96.00% was achieved across classes using standard personal computers, with the lowest class-wise accuracy still reaching a notable 89.00%. The accuracies of the ML model for the four classes using different sources of data are summarised in *Table 6.* The model's accuracy can be still improved by exploiting more advanced computing resources and/or larger datasets. By transforming the GW responses into time-frequency scalograms and applying transfer learning, the proposed ML framework was made inherently robust to any residual noise present in the experimental study.

Table 6*. Summary of the ML model performance.*

Category	Class H	Class ED	Class LD	Class TD	Class-wise average
Experimental data	100.00%	97.25%	97.25%	89.00%	95.88%
Simulated data	100.00%	98.00%	98.75%	90.00%	96.69%
Mean	100.00%	97.63%	98.00%	89.50%	96.28%

6. Conclusions

The present work focuses on developing and validating the GW-ML framework using laboratory-scale blade specimens and FE simulations. While early-warning models for specific damage modes are not explicitly provided here, the two-stage classifier already demonstrates capability in distinguishing erosion, longitudinal debonding, and transverse debonding from pristine conditions. This lays the foundation for mode-specific damage indicators, which can be further enhanced in future studies by incorporating progression trends or statistical thresholds for early detection.

This research presents a data-driven structural health monitoring (SHM) framework for wind turbine blades (WTBs), integrating guided wave (GW) sensing with a customised machine learning (ML) model. The system combines experimental and simulated data to enable accurate and efficient damage detection and categorisation.

- Laboratory experiments, supported by FE simulations using a triple-array sensor setup, provided comprehensive datasets. The alignment between numerical and experimental results validated the model's predictive reliability and improved detection sensitivity.

- GW signals were converted into RGB scalograms to extract time-frequency features, enabling clear differentiation of damage types and enhancing classification accuracy.

- These scalograms were used to train a tailored ML model, which achieved high accuracy and robustness in identifying both the presence and type of damage. The model's performance was assessed through multiple test runs and confidence interval analyses, demonstrated strong consistency.

- Transfer learning (TL) further improved model efficiency by reducing training time and data dependency, supporting scalability for real-world applications.

The proposed approach offers a reliable and generalisable solution for condition monitoring in wind turbines. Its adaptability also extends to other sectors, such as aerospace and automotive. Although the present work does not directly demonstrate transfer from laboratory to in-field turbine operation, the choice of TL is motivated by scalability. By leveraging pre-trained representations and combining experimental and simulated data during training, the proposed framework is designed to be adaptable for future deployment under real operational conditions.

The designed framework demonstrates strong performance on laboratory-scale specimens, although its current validation is limited to controlled conditions, stationary blades, and a restricted range of damage scenarios. Full-scale deployment will require additional studies incorporating environmental variability, operational loading scenarios, and long-term monitoring policies. Furthermore, while the combination of experimental and simulated data improves generalisability, the fidelity of the ML model ultimately depends on the breadth and representativeness of the training datasets.

Regarding scalability, the data from small-scale blades cannot be directly extrapolated to full-scale turbines without further validation. However, the framework itself is generalisable: by retraining the ML model with datasets obtained from large-scale experimental studies and in-service operational monitoring (including ambient and loading conditions), the methodology can be adapted for real-world applications. The current study therefore serves as a proof-of-concept, demonstrating that the approach is computationally efficient, robust, and extendable to industrial-scale SHM systems.

Future work will focus on deploying an advanced smart sensing platform using ultrasonic responses for in-situ monitoring of operational turbines.

Acknowledgement

Authors wish to acknowledge the support from the University of Huddersfield, URF Grant: QR24E025.

Statements and declarations

Authors have no financial or non-financial competing interests to declare that are relevant to the content of this article.

References

[1] IEA, ‘Renewables 2024 - Analysis and forecast to 2030’, 2025. Accessed: Jun. 03, 2025. [Online]. Available: https://www.iea.org/reports/renewables-2024

[2] GWEC, ‘Global Wind Report 2025’, 2025. Accessed: Jun. 03, 2025. [Online]. Available: https://www.gwec.net/reports/globalwindreport

[3] X. Ding, Y. Gong, C. Wang, and Z. Zheng, ‘Artificial intelligence based abnormal detection system and method for wind power equipment’, *International Journal of Thermofluids*, vol. 21, p. 100569, Feb. 2024, doi: 10.1016/J.IJFT.2024.100569.

[4] Q. Wang, J. Hu, S. Yang, Z. Dong, X. Deng, and Y. Xu, ‘Towards machine learning applications for structural load and power assessment of wind turbine: An engineering perspective’, *Energy Convers Manag*, vol. 324, p. 119275, Jan. 2025, doi: 10.1016/j.enconman.2024.119275.

[5] Y.-T. Wu and F. Porté-Agel, ‘Modeling turbine wakes and power losses within a wind farm using LES: An application to the Horns Rev offshore wind farm’, *Renew Energy*, vol. 75, pp. 945–955, Mar. 2015, doi: 10.1016/j.renene.2014.06.019.

[6] A. Sebastiani, F. Castellani, G. Crasto, and A. Segalini, ‘Data analysis and simulation of the Lillgrund wind farm’, *Wind Energy*, vol. 24, no. 6, pp. 634–648, Jun. 2021, doi: 10.1002/we.2594.

[7] C. L. Archer *et al.*, ‘Review and evaluation of wake loss models for wind energy applications’, *Appl Energy*, vol. 226, pp. 1187–1207, Sep. 2018, doi: 10.1016/j.apenergy.2018.05.085.

[8] X. Wang, Y. Wang, and Y. Liu, ‘Dynamic load frequency control for high-penetration wind power considering wind turbine fatigue load’, *International Journal of Electrical Power & Energy Systems*, vol. 117, p. 105696, May 2020, doi: 10.1016/j.ijepes.2019.105696.

[9] J. Izquierdo, A. C. Márquez, J. Uribetxebarria, and A. Erguido, ‘On the importance of assessing the operational context impact on maintenance management for life cycle cost of wind energy projects’, *Renew Energy*, vol. 153, pp. 1100–1110, Jun. 2020, doi: 10.1016/J.RENENE.2020.02.048.

[10] L. Mishnaevsky, K. Branner, H. Petersen, J. Beauson, M. McGugan, and B. Sørensen, ‘Materials for Wind Turbine Blades: An Overview’, *Materials*, vol. 10, no. 11, p. 1285, Nov. 2017, doi: 10.3390/ma10111285.

[11] K. Kong, K. Dyer, C. Payne, I. Hamerton, and P. M. Weaver, ‘Progress and Trends in Damage Detection Methods, Maintenance, and Data-driven Monitoring of Wind Turbine Blades – A Review’, *Renewable Energy Focus*, vol. 44, pp. 390–412, Mar. 2023, doi: 10.1016/J.REF.2022.08.005.

[12] L. M. Martulli, M. Diani, G. Sabetta, S. Bontumasi, M. Colledani, and A. Bernasconi, ‘Critical review of current wind turbine blades’ design and materials and their influence on the end-of-life management of wind turbines’, *Eng Struct*, vol. 327, p. 119625, Mar. 2025, doi: 10.1016/J.ENGSTRUCT.2025.119625.

[13] M. Dimitrova, A. Aminzadeh, M. S. Meiabadi, S. Sattarpanah Karganroudi, H. Taheri, and H. Ibrahim, ‘A Survey on Non-Destructive Smart Inspection of Wind Turbine Blades Based on Industry 4.0 Strategy’, *Applied Mechanics*, vol. 3, no. 4, pp. 1299–1326, Nov. 2022, doi: 10.3390/applmech3040075.

[14] M. A. Oliveira, E. F. Simas Filho, M. C. S. Albuquerque, Y. T. B. Santos, I. C. da Silva, and C. T. T. Farias, 'Ultrasound-based identification of damage in wind turbine blades using novelty detection', *Ultrasonics*, vol. 108, p. 106166, Dec. 2020, doi: 10.1016/J.ULTRAS.2020.106166.

[15] T. M. Naqash and Md. M. Alam, 'A State-of-the-Art Review of Wind Turbine Blades: Principles, Flow-Induced Vibrations, Failure, Maintenance, and Vibration Suppression Techniques', *Energies (Basel)*, vol. 18, no. 13, p. 3319, Jun. 2025, doi: 10.3390/en18133319.

[16] K. Kong, K. Dyer, C. Payne, I. Hamerton, and P. M. Weaver, 'Progress and Trends in Damage Detection Methods, Maintenance, and Data-driven Monitoring of Wind Turbine Blades – A Review', *Renewable Energy Focus*, vol. 44, pp. 390–412, Mar. 2023, doi: 10.1016/J.REF.2022.08.005.

[17] Y. Tong *et al.*, 'Materials Design and Structural Health Monitoring of Horizontal Axis Offshore Wind Turbines: A State-of-the-Art Review', *Materials*, vol. 18, no. 2, p. 329, Jan. 2025, doi: 10.3390/ma18020329.

[18] Y. Du, S. Zhou, X. Jing, Y. Peng, H. Wu, and N. Kwok, 'Damage detection techniques for wind turbine blades: A review', *Mech Syst Signal Process*, vol. 141, p. 106445, Jul. 2020, doi: 10.1016/J.YMSSP.2019.106445.

[19] S. Ding, C. Yang, and S. Zhang, 'Acoustic-Signal-Based Damage Detection of Wind Turbine Blades-A Review', *Sensors*, vol. 23, no. 11, p. 4987, May 2023, doi: 10.3390/s23114987.

[20] F. Brinkschmidt, 'Technologies for structural health monitoring of wind turbine blades - An overview of different techniques', *Educational Journal of Renewable Energy Short Reviews*, vol. 2024, no. 03, pp. 14–21, Jan. 2024, doi: https://doi.org/10.25974/ren_rev_2024_03.

[21] J. W. Barker, N. Bhowmik, and T. P. Breckon, 'Semi-Supervised Surface Anomaly Detection of Composite Wind Turbine Blades From Drone Imagery', in *17th International Conference on Computer Vision Theory and Applications (VISAPP)*, 2022.

[22] S.-J. Heo and W. S. Na, 'Review of Drone-Based Technologies for Wind Turbine Blade Inspection', *Electronics (Basel)*, vol. 14, no. 2, p. 227, Jan. 2025, doi: 10.3390/electronics14020227.

[23] C. Humer, S. Höll, C. Kralovec, and M. Schagerl, 'Damage identification using wave damage interaction coefficients predicted by deep neural networks', *Ultrasonics*, vol. 124, p. 106743, Aug. 2022, doi: 10.1016/J.ULTRAS.2022.106743.

[24] P. A. Kalgutkar and S. Banerjee, 'Interaction of ultrasonic guided waves with interfacial debonding in a stiffened composite plate under variable temperature and operational conditions', *Ultrasonics*, vol. 142, p. 107378, Aug. 2024, doi: 10.1016/j.ultras.2024.107378.

[25] P. Kashyap *et al.*, 'Unsupervised deep learning framework for temperature-compensated damage assessment using ultrasonic guided waves on edge device', *Sci Rep*, vol. 14, no. 1, p. 3751, Feb. 2024, doi: 10.1038/s41598-024-54418-w.

[26] C. Kralovec and M. Schagerl, 'Review of Structural Health Monitoring Methods Regarding a Multi-Sensor Approach for Damage Assessment of Metal and Composite Structures', *Sensors*, vol. 20, no. 3, p. 826, Feb. 2020, doi: 10.3390/s20030826.

[27] G. Sha, H. Xu, M. Radzieński, M. Cao, W. Ostachowicz, and Z. Su, 'Guided wavefield curvature imaging of invisible damage in composite structures', *Mech Syst Signal Process*, vol. 150, p. 107240, Mar. 2021, doi: 10.1016/j.ymssp.2020.107240.

[28] Z. Su, L. Ye, and Y. Lu, 'Guided Lamb waves for identification of damage in composite structures: A review', *J Sound Vib*, vol. 295, no. 3–5, pp. 753–780, Aug. 2006, doi: 10.1016/j.jsv.2006.01.020.

[29] S. Sikdar, P. Fiborek, P. Kudela, S. Banerjee, and W. Ostachowicz, ‘Effects of debonding on Lamb wave propagation in a bonded composite structure under variable temperature conditions’, *Smart Mater Struct*, vol. 28, no. 1, p. 015021, Jan. 2019, doi: 10.1088/1361-665X/aaefaa.

[30] A. De Luca, D. Perfetto, G. Lamanna, A. Aversano, and F. Caputo, ‘Numerical Investigation on Guided Waves Dispersion and Scattering Phenomena in Stiffened Panels’, *Materials*, vol. 15, no. 1, p. 74, Dec. 2021, doi: 10.3390/ma15010074.

[31] V. Memmolo, E. Monaco, N. D. Boffa, L. Maio, and F. Ricci, ‘Guided wave propagation and scattering for structural health monitoring of stiffened composites’, *Compos Struct*, vol. 184, pp. 568–580, Jan. 2018, doi: 10.1016/j.compstruct.2017.09.067.

[32] F. Ciampa, S. G. Pickering, G. Scarselli, and M. Meo, ‘Nonlinear imaging of damage in composite structures using sparse ultrasonic sensor arrays’, *Struct Control Health Monit*, vol. 24, no. 5, p. e1911, May 2017, doi: 10.1002/stc.1911.

[33] F. Ciampa and M. Meo, ‘Nonlinear elastic imaging using reciprocal time reversal and third order symmetry analysis’, *J Acoust Soc Am*, vol. 131, no. 6, pp. 4316–4323, Jun. 2012, doi: 10.1121/1.4707522.

[34] K. Yang, J. A. Rongong, and K. Worden, ‘Damage detection in a laboratory wind turbine blade using techniques of ultrasonic NDT and SHM’, *Strain*, vol. 54, no. 6, Dec. 2018, doi: 10.1111/str.12290.

[35] S. Shoja, V. Berbyuk, and A. Boström, ‘Guided wave–based approach for ice detection on wind turbine blades’, *Wind Engineering*, vol. 42, no. 5, pp. 483–495, Oct. 2018, doi: 10.1177/0309524X18754767.

[36] R. Raišutis, K. A. Tiwari, E. Žukauskas, O. Tumšys, and L. Draudvilienė, ‘A Novel Defect Estimation Approach in Wind Turbine Blades Based on Phase Velocity Variation of Ultrasonic Guided Waves’, *Sensors*, vol. 21, no. 14, p. 4879, Jul. 2021, doi: 10.3390/s21144879.

[37] A. Kundu, S. Sikdar, M. Eaton, and R. Navaratne, ‘A Generic Framework for Application of Machine Learning in Acoustic Emission-Based Damage Identification’, in *Proceedings of the 13th International Conference on Damage Assessment of Structures.*, Lecture Notes in Mechanical Engineering. Springer, 2020, pp. 244–262. doi: 10.1007/978-981-13-8331-1_18.

[38] A. Movsessian, D. García Cava, and D. Tcherniak, ‘An artificial neural network methodology for damage detection: Demonstration on an operating wind turbine blade’, *Mech Syst Signal Process*, vol. 159, p. 107766, Oct. 2021, doi: 10.1016/J.YMSSP.2021.107766.

[39] S. Sikdar and J. Pal, ‘Bag of visual words based machine learning framework for disbond characterisation in composite sandwich structures using guided waves’, *Smart Mater Struct*, vol. 30, no. 7, p. 075016, Jul. 2021, doi: 10.1088/1361-665X/ac01a8.

[40] S. Hoell and P. Omenzetter, ‘Fukunaga-Koontz feature transformation for statistical structural damage detection and hierarchical neuro-fuzzy damage localisation’, *J Sound Vib*, vol. 400, pp. 329–353, Jul. 2017, doi: 10.1016/J.JSV.2017.03.048.

[41] C. Sbarufatti, G. Manson, and K. Worden, ‘A numerically-enhanced machine learning approach to damage diagnosis using a Lamb wave sensing network’, *J Sound Vib*, vol. 333, no. 19, pp. 4499–4525, Sep. 2014, doi: 10.1016/J.JSV.2014.04.059.

[42] B. F. Junqueira, R. Leiderman, and D. A. Castello, ‘Damage recovery in composite laminates through deep learning from acoustic scattering of guided waves’, *Ultrasonics*, vol. 139, p. 107293, Apr. 2024, doi: 10.1016/j.ultras.2024.107293.

[43] L. Cappugi, A. Castorrini, A. Bonfiglioli, E. Minisci, and M. S. Campobasso, ‘Machine learning-enabled prediction of wind turbine energy yield losses due to general blade leading edge erosion’, *Energy Convers Manag*, vol. 245, p. 114567, Oct. 2021, doi: 10.1016/J.ENCONMAN.2021.114567.

[44] Q. Yuan, Y. Wang, Z. Su, and T. Zhang, ‘Quantitative damage evaluation of curved plates based on phased array guided wave and deep learning algorithm’, *Ultrasonics*, vol. 137, p. 107176, Feb. 2024, doi: 10.1016/J.ULTRAS.2023.107176.

[45] W. Wu *et al.*, ‘Guided waves-based damage identification in plates through an inverse Bayesian process’, *Ultrasonics*, vol. 125, p. 106773, Sep. 2022, doi: 10.1016/j.ultras.2022.106773.

[46] J. Lu, Y. Zheng, H. Zhang, and Y. Cao, ‘Bayesian approach of elliptical loci and RAPID for damage localization in wind turbine blade’, *Smart Mater Struct*, vol. 33, no. 4, p. 045008, Apr. 2024, doi: 10.1088/1361-665X/ad2f0b.

[47] S. Xue, W. Zhou, J. L. Beck, Y. Huang, and H. Li, ‘Damage localization and robust diagnostics in guided-wave testing using multitask complex hierarchical sparse Bayesian learning’, *Mech Syst Signal Process*, vol. 197, p. 110365, Aug. 2023, doi: 10.1016/J.YMSSP.2023.110365.

[48] S. LIU, Q. LI, B. LU, and J. HE, ‘Prediction of offshore wind turbine wake and output power using large eddy simulation and convolutional neural network’, *Energy Convers Manag*, vol. 324, p. 119326, Jan. 2025, doi: 10.1016/J.ENCONMAN.2024.119326.

[49] F. Ye and A. A. Ezzat, ‘Icing detection and prediction for wind turbines using multivariate sensor data and machine learning’, *Renew Energy*, vol. 231, p. 120879, Sep. 2024, doi: 10.1016/j.renene.2024.120879.

[50] I. Lapczyk and J. A. Hurtado, ‘Progressive damage modeling in fiber-reinforced materials’, *Compos Part A Appl Sci Manuf*, vol. 38, no. 11, pp. 2333–2341, Nov. 2007, doi: 10.1016/j.compositesa.2007.01.017.

[51] A. Matzenmiller, J. Lubliner, and R. L. Taylor, ‘A constitutive model for anisotropic damage in fiber-composites’, *Mechanics of Materials*, vol. 20, no. 2, pp. 125–152, Apr. 1995, doi: 10.1016/0167-6636(94)00053-0.

[52] C. B. Pol and S. Banerjee, ‘Modeling and analysis of propagating guided wave modes in a laminated composite plate subject to transient surface excitations’, *Wave Motion*, vol. 50, no. 5, pp. 964–978, Jul. 2013, doi: 10.1016/j.wavemoti.2013.04.003.

[53] L. Bek, R. Kottner, and V. Laš, ‘Material model for simulation of progressive damage of composite materials using 3D Puck failure criterion’, *Compos Struct*, vol. 259, p. 113435, 2021, doi: https://doi.org/10.1016/j.compstruct.2020.113435.

[54] A. A. and N. A. V. and S. B. and R. A. Reddy K. S. S. and Nasedkina, ‘Comparative Study on Progressive Damage Models for Composites’, in *Advanced Materials* , S.-H. and G. V. K. Parinov Ivan A. and Chang, Ed., Cham: Springer International Publishing, 2018, pp. 413–427.

[55] Abaqus/CAE, ‘Delamination analysis of laminated composites’, Massachusetts Institute of Technology (MIT). Accessed: Apr. 16, 2025. [Online]. Available: https://abaqus-docs.mit.edu/2017/English/SIMACAEBMKRefMap/simabmk-c-alfanodelamination.htm

[56] S. M. Barr and J. W. Jaworski, ‘Optimization of tow-steered composite wind turbine blades for static aeroelastic performance’, *Renew Energy*, vol. 139, pp. 859–872, Aug. 2019, doi: 10.1016/J.RENENE.2019.02.125.

[57] K. Simonyan and A. Zisserman, ‘Very Deep Convolutional Networks for Large-Scale Image Recognition’, Sep. 2014, Accessed: Jul. 11, 2025. [Online]. Available: https://arxiv.org/abs/1409.1556

[58] J. Ren and H. Wang, ‘Calculus and optimization’, in *Mathematical Methods in Data Science*, Elsevier, 2023, pp. 51–89. doi: 10.1016/B978-0-44-318679-0.00009-0.

[59] Z. Wang, W. Yan, and T. Oates, ‘Time series classification from scratch with deep neural networks: A strong baseline’, in *2017 International Joint Conference on Neural Networks (IJCNN)*, IEEE, May 2017, pp. 1578–1585. doi: 10.1109/IJCNN.2017.7966039.

[60] T. Guo, L. Wu, C. Wang, and Z. Xu, ‘Damage detection in a novel deep-learning framework: a robust method for feature extraction’, *Struct Health Monit*, vol. 19, no. 2, pp. 424–442, Mar. 2020, doi: 10.1177/1475921719846051.

[61] G. Jiang, R. Yue, Q. He, P. Xie, and X. Li, ‘Imbalanced learning for wind turbine blade icing detection via spatio-temporal attention model with a self-adaptive weight loss function’, *Expert Syst Appl*, vol. 229, p. 120428, Nov. 2023, doi: 10.1016/J.ESWA.2023.120428.

[62] N. Gueorguieva, I. Valova, and D. Klusek, ‘Solving Large Scale Classification Problems with Stochastic Based Optimization’, *Procedia Comput Sci*, vol. 168, pp. 26–33, 2020, doi: 10.1016/j.procs.2020.02.247.

[63] A. Tavares, E. Di Lorenzo, B. Cornelis, B. Peeters, W. Desmet, and K. Gryllias, ‘Machine Learning approaches to damage detection in composite structures combining experimental and simulation domains’, *Mech Syst Signal Process*, vol. 215, p. 111412, Jun. 2024, doi: 10.1016/J.YMSSP.2024.111412.

[64] S. Sikdar, A. Gullapalli, and A. Kundu, ‘A hierarchical multistage holistic model for acoustic emission source monitoring in composites’, *Smart Mater Struct*, vol. 33, no. 11, p. 115022, Nov. 2024, doi: 10.1088/1361-665X/ad8409.